

# In Situ Designing a Gradient Li<sup>+</sup> Capture and Quasi-Spontaneous Diffusion Anode Protection Layer toward Long-Life Li–O<sub>2</sub> Batteries

Yue Yu, Gang Huang, Jia-Zhi Wang, Kai Li, Jin-Ling Ma, and Xin-Bo Zhang\*

Lithium metal is the only anode material that can enable the Li–O<sub>2</sub> battery to realize its high theoretical energy density ( $\approx 3500 \text{ Wh kg}^{-1}$ ). However, the inherent uncontrolled dendrite growth and serious corrosion limitations of lithium metal anodes make it experience fast degradation and impede the practical application of Li–O<sub>2</sub> batteries. Herein, a multifunctional complementary LiF/F-doped carbon gradient protection layer on a lithium metal anode by one-step in situ reaction of molten Li with poly(tetrafluoroethylene) (PTFE) is developed. The abundant strong polar C–F bonds in the upper carbon can not only act as Li<sup>+</sup> capture site to pre-uniform Li<sup>+</sup> flux but also regulate the electron configuration of LiF to make Li<sup>+</sup> quasi-spontaneously diffuse from carbon to LiF surface, avoiding the strong Li<sup>+</sup>-adhesion-induced Li aggregation. For LiF, it can behave as fast Li<sup>+</sup> conductor and homogenize the nucleation sites on lithium, as well as ensure firm connection with lithium. As a result, this well-designed protection layer endows the Li metal anode with dendrite-free plating/stripping and anticorrosion behavior both in ether-based and carbonate ester-based electrolytes. Even applied protected Li anodes in Li–O<sub>2</sub> batteries, its superiority can still be maintained, making the cell achieve stable cycling performance (180 cycles).

The energy densities of current commercial Li-ion batteries (LIBs) are approaching their achievable limit and restrict the rapid development of electric vehicles and smart grid storage.<sup>[1–6]</sup> To this end, Li–O<sub>2</sub> battery with ultrahigh theoretical energy density ( $\approx 3500 \text{ Wh kg}^{-1}$ ) increasingly draws the scientists'

Y. Yu, J.-Z. Wang, K. Li, Prof. X.-B. Zhang  
State Key Laboratory of Rare Earth Resource Utilization  
Changchun Institute of Applied Chemistry  
Chinese Academy of Sciences  
Changchun 130022, P. R. China  
E-mail: xbzhang@ciac.ac.cn

Y. Yu, J.-Z. Wang, Prof. X.-B. Zhang  
University of Science and Technology of China  
Hefei 230026, P. R. China

Dr. G. Huang  
Physical Science and Engineering Division  
King Abdullah University of Science and Technology  
Thuwal 23955-6900, Saudi Arabia

Dr. J.-L. Ma  
School of Electrical Engineering  
Chongqing University  
174 Shazheng Street, Shapingba District, Chongqing 400044, P. R. China

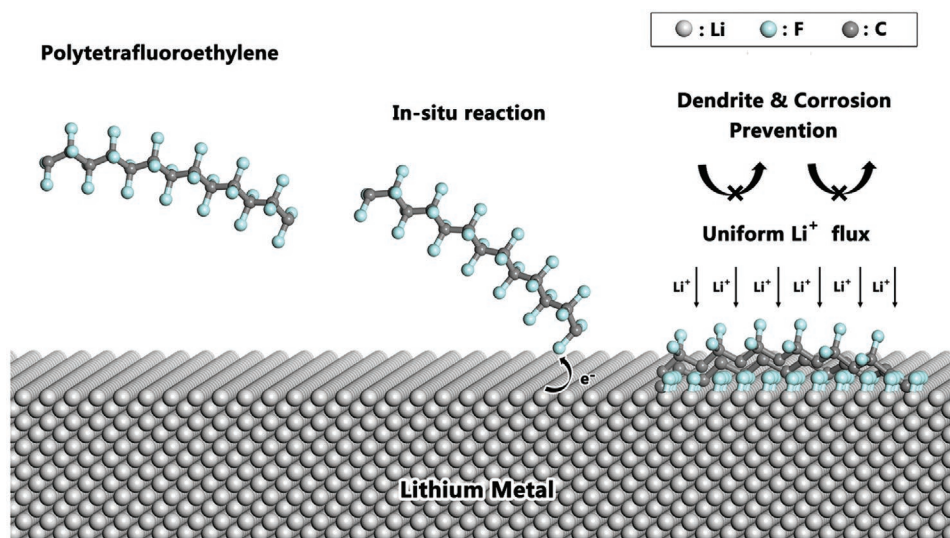
 The ORCID identification number(s) for the author(s) of this article can be found under <https://doi.org/10.1002/adma.202004157>.

DOI: 10.1002/adma.202004157

attention and has been regarded as a promising next-generation energy storage system to substitute LIBs.<sup>[7–9]</sup> However, the Li–O<sub>2</sub> battery confronts with plenty of challenges, such as electrolyte decomposition, cathode failure, and anode degradation.<sup>[10–12]</sup> In the past decade, most of the efforts have been devoted to improve the stability and effectiveness of the electrolyte and cathode, while the importance of the lithium anode protection has long been ignored, making the long-term operation of Li–O<sub>2</sub> battery become impossible. Since lithium possesses the highest theoretical specific capacity ( $3860 \text{ mAh g}^{-1}$ ) and lowest redox potential ( $-3.04 \text{ V}$  versus standard hydrogen electrode), it is irreplaceable and also the only candidate anode in enabling Li–O<sub>2</sub> battery to deliver the maximum energy density.<sup>[13–15]</sup> Nevertheless, the highly active nature of lithium and the uncontrollable lithium dendrite growth during cycling will constantly expose new lithium and continuously

react with the electrolyte and “contaminants” (H<sub>2</sub>O, O<sub>2</sub>, strong oxidizing reaction intermediates) in Li–O<sub>2</sub> batteries, causing lithium experiences serious corrosion and quick exhaustion, thus severely deteriorating the cycling stability of Li–O<sub>2</sub> batteries and limiting their practical applications.<sup>[16–19]</sup> Therefore, except optimization of the electrolyte and cathode, it is urgent and crucial to resolve the Li anode associated issues so as to further improve the electrochemical performance of Li–O<sub>2</sub> batteries.

It has been demonstrated that designing 3D porous lithium host is an effective method to prevent lithium dendrite growth in LIBs.<sup>[20–21]</sup> However, unlike the close and non-gas involving system of LIBs, the high specific surface area of the 3D host will make lithium expose more corrosion reaction sites in the semi-open Li–O<sub>2</sub> batteries, consequently accelerating the consumption of active lithium and battery failure. To avoid this high surface area induced adverse effects, surface modification of the bare lithium sheet is a powerful solution. Among the various strategies used to modify the lithium surface, electrolyte regulation has been widely adopted to build a stable solid electrolyte interphase (SEI) film on lithium for inhibiting dendrite growth. For example, the electrolyte regulation can facilitate the formation of LiF-riched SEI layer, which is effective to restrict dendrite growth and parasitic side reactions.<sup>[22]</sup> Despite efficient, the formation of the SEI film is usually accompanied with



**Scheme 1.** Schematic illustration of the design guideline of PTL. (Here, we use the 15<sub>h</sub> helix configuration of PTFE to stand for the PTFE molecule).<sup>[40]</sup>

the decomposition of the electrolyte solvent, which makes the SEI compose of multiple components with diverse  $\text{Li}^+$  conductivities, consequently, inducing different lithium plating/stripping behaviors at different areas and eventually SEI rupture, that is, this method will become invalid in the long run. In contrast, directly constructing artificial protection layer on lithium can avert this disadvantage, because the layer composition can be accurately designed and controlled.<sup>[11,16]</sup> An ideal artificial protection layer should simultaneously possess the functions of homogenizing the  $\text{Li}^+$  flux at the electrode/electrolyte interface and enabling fast  $\text{Li}^+$  diffusion. Previous results revealed that LiF could act as a main effective component in the protection layer for inhibiting lithium dendrite growth because of the multifunctional protection effects it brought. The high interfacial energy and low  $\text{Li}^+$  surface diffusion barrier of LiF can guide uniform lithium deposition and reduce uncontrollable dendrite growth,<sup>[22]</sup> while its large bandgap (13.6 eV) can assist to block electron tunneling through the protection layer, which is beneficial for minimizing the occurrence of corrosion reactions.<sup>[23]</sup> Besides, LiF also has a wide electrochemical stability window and a high shear modulus (55.1 GPa),<sup>[24,25]</sup> avoiding the high voltage induced decomposition and lithium dendrite caused protection layer breakage. At present, the only limitation of LiF to be a prospective artificial protection layer is its weak adsorption ability to  $\text{Li}^+$ , which can not homogenize surface  $\text{Li}^+$  flux, as a result, there is a possibility leading to nonuniform Li deposition. For homogenizing the surface  $\text{Li}^+$  flux, carbon based materials have unique advantages due to their adjustable electronic structure by heteroatom doping.<sup>[26–28]</sup> For example, the introduction of N-containing function groups into the graphene can increase its binding energy to  $\text{Li}^+$ , so that preuniforming the  $\text{Li}^+$  flux before deposition.<sup>[21]</sup> Moreover, carbon materials can also work as physical barrier to retard corrosion reactions between lithium, electrolyte, and “contaminants.”<sup>[29–31]</sup> However, it should be noted that the  $\text{Li}^+$  binding energies of the polar functional groups in the carbon materials are usually too strong that renders the  $\text{Li}^+$  directly get an  $\text{e}^-$  and deposit on the carbon

surface rather than diffuse through the carbon layer to reach the lithium surface. This newly deposited lithium will expose to the electrolyte and “contaminants” again and experience serious corrosion. To date, there is no artificial protection layer that can homogenize the  $\text{Li}^+$  flux while allowing fast  $\text{Li}^+$  diffusion. If we can combine the homogenizing  $\text{Li}^+$  flux function of carbon materials with the fast  $\text{Li}^+$  diffusion ability of LiF together to make an integrated protection layer, the lithium associated issues in Li– $\text{O}_2$  batteries will be undoubtedly resolved.

With this in mind, herein, we designed an in situ one-step reaction between molten Li and poly(tetrafluoroethylene) (PTFE) for constructing a multifunctional complementary LiF/F-doped carbon gradient protection layer that firmly coated on lithium anode surface. The upper rich F-doped carbon can act as  $\text{Li}^+$  capturing sites to preuniform  $\text{Li}^+$  distribution and regulate the electron configuration of LiF to increase its binding energy to  $\text{Li}^+$  and assist  $\text{Li}^+$  almost spontaneously migrate from the carbon to the  $\text{Li}^+$  conductive LiF with lithium only deposited on the protection layer/Li interface (**Scheme 1**). This protection layer integrates the high  $\text{Li}^+$  adsorption surface and fast  $\text{Li}^+$  diffusion bulk together, as a consequence, it enables dendrite-free lithium plating/stripping with a lower nucleation overpotential, guarantees a stable electrode/electrolyte interface, and facilitates faster electrochemical and mass transport kinetics in both ether-based and carbonate ester based electrolytes. With these benefits as well as the corrosion-resistant ability, the protected lithium anode prolongs the lifetime of Li– $\text{O}_2$  battery to 180 cycles, more than two times that of the cell using bare lithium anode (78 cycles).

As schematically illustrated in **Figure 1a**, a dual-phase LiF/F-doped carbon protection layer with abundant strong polar C–F bonds in the upper side can be quickly and easily obtained via in situ one-step reaction between PTFE micropowders and lithium sheet. For convenience, hereinafter, the abbreviation “BL” stands for bare lithium, “PTL” refers to the lithium metal anode after protection and “PT layer” stands for the as-prepared protection layer. Under argon atmosphere at 300 °C, the molten lithium sheet reacts with PTFE micropowders to generate

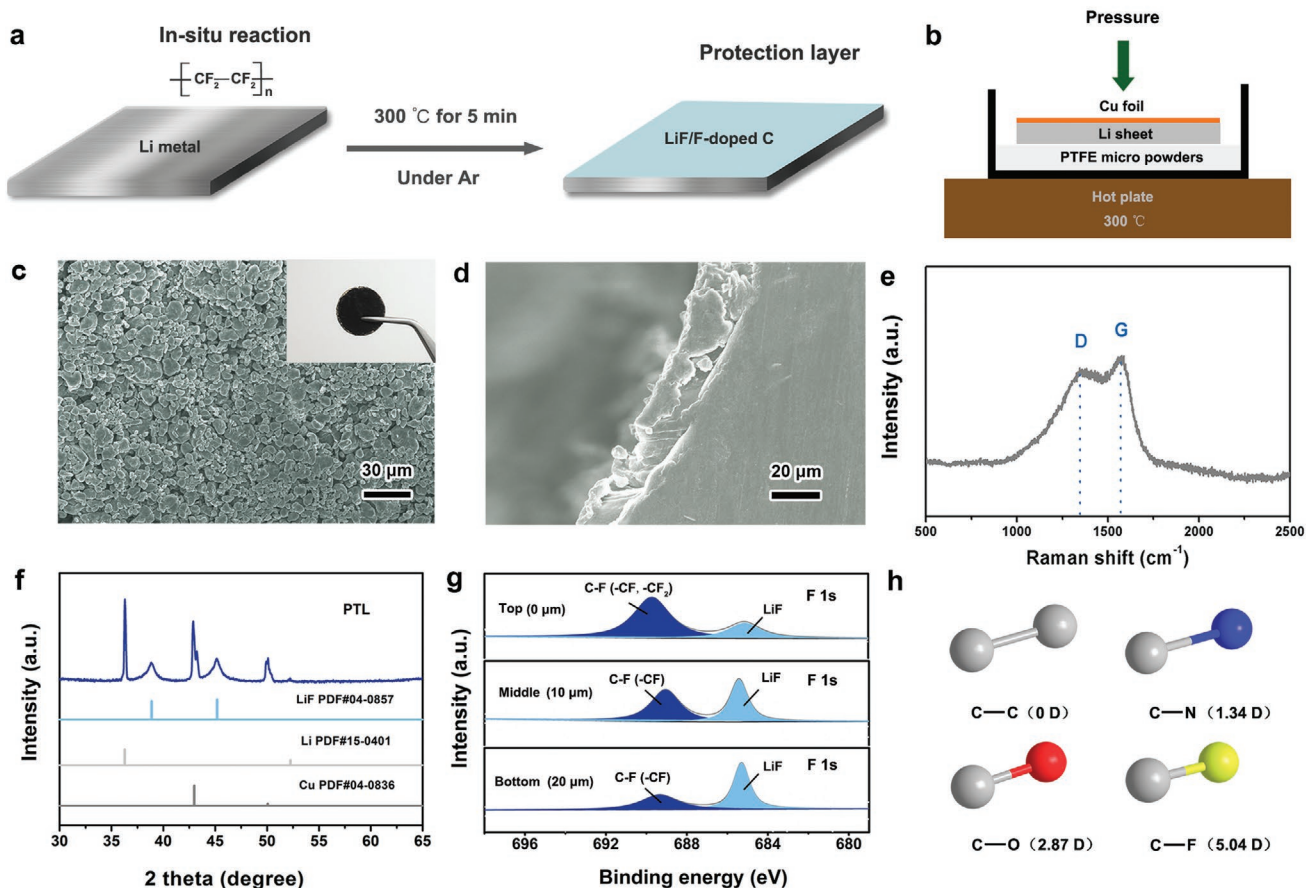


**Figure 1.** a,b) Schematic illustrations of the film formation reaction (a) and preparation process of PTL (b). c) Surface SEM image of PTL. Inset is the optical image of PTL. d) Cross-section SEM image of PTL. e) Raman spectrum and f) X-ray diffraction (XRD) curves of PTL. g) F 1s X-ray photoelectron spectroscopy (XPS) spectra of PTL at different depths. h) Dipole moment of C–C, C–N, C–O, and C–F.

two phases as Equation (1) indicated—a Li atom bonds with a F atom to produce LiF and the rest of the C atoms will form carbon (Figure 1b). To demonstrate the morphology and chemistry composition of the PT layer, scanning electron microscopy (SEM), X-ray photoelectron spectroscopy (XPS), X-ray diffraction (XRD), and Raman spectra were employed. It can be seen from Figure 1c,d that the as-prepared black color PT layer is seamlessly connected to the lithium sheets and displays a uniform surface morphology with a thickness about 20  $\mu\text{m}$ . As expected, the Raman spectrum (Figure 1e) verifies the existence of carbon and the LiF phase in the XRD curves (Figure 1f and Figure S1, Supporting Information) confirms the formation of LiF in the PT layer. These are in accord with the proposed reaction equation. In addition, the F 1s XPS spectra reveals that the carbon is functionalized with F element and the content of F-doped C decreases with the increase of depth, while the LiF exhibits opposite trend, indicating the richness of the F-doped carbon in the top side and the LiF in the bottom side of the PT layer (Figure 1g). Due to the existence of unreacted  $-\text{CF}_2$ , the wider binding energy of the C–F peak can be found in the XPS results of the top species. It is worth mentioning that the strong polar electron-rich C–F bonds in the F-doped carbon can perform as effective Lewis base sites to adsorb Lewis acidic  $\text{Li}^+$  and homogenize the  $\text{Li}^+$  flux (Figure 1h).<sup>[32]</sup>



With the successful synthesis of PT layer, we then evaluated the nucleation energy barrier of lithium on the PTL by checking the Li nucleation overpotential during lithium deposition process. For comparison, the same lithium source was used to deposit lithium onto the BL and PTL in carbonate ester based electrolyte. Generally, the nucleation overpotential ( $\mu_n$ ) and the plateau overpotential ( $\mu_p$ ) are related to the energy barrier of heterogeneous nucleation process and mass-transfer process,<sup>[33]</sup> respectively. As indicated in Figure 2a, for BL, the voltage drops to  $-0.227 \text{ V}$  at the initial stage of nucleation and then reaches a plateau at  $-0.1046 \text{ V}$  under a current density of  $3 \text{ mA cm}^{-2}$ . By contrast, the voltage dip on PTL is only  $-0.1562 \text{ V}$  and stabilizes at  $-0.0794 \text{ V}$  during subsequent lithium growth process (Figure 2b). Even under a higher current density of  $5 \text{ mA cm}^{-2}$ , the  $\mu_n$  (0.1302 V) and  $\mu_p$  (0.1276 V) on PTL are still much lower than the  $\mu_n$  (0.1801 V) and  $\mu_p$  (0.1406 V) on BL (Figure S2, Supporting Information). Besides, lower  $\mu_n$  (0.0057 V) and  $\mu_p$  (0.0321 V) are also achieved on PTL with ether-based electrolyte (Figure S3, Supporting Information). These obvious reductions of  $\mu_n$  and  $\mu_p$  in both the carbonate ester based and ether-based electrolytes can be explained by the reduced energy barrier of lithium nucleation and growth steps with the assistance of PT layer.

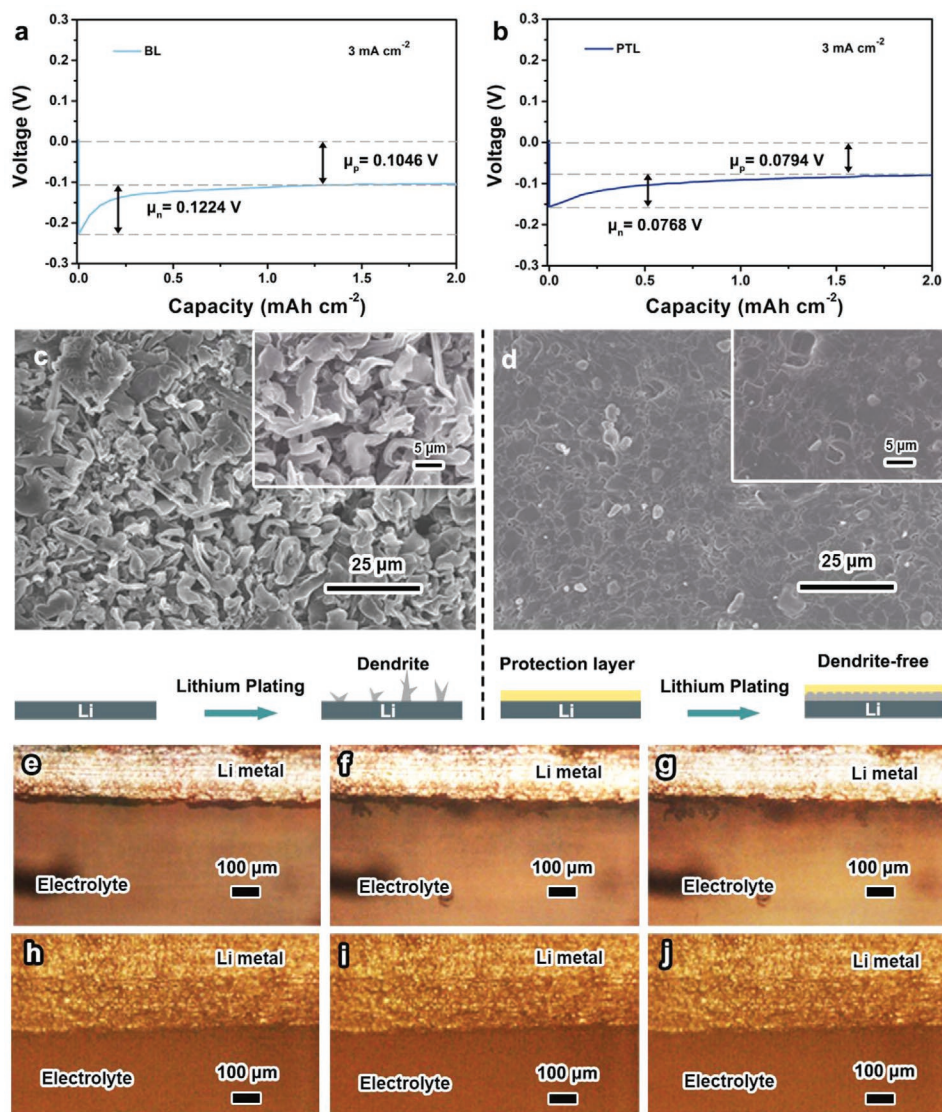


**Figure 2.** a,b) Voltage–capacity curves of Li plating on BL (a) and PTL (b) at a current density of 3 mA cm<sup>-2</sup>. c,d) SEM images and corresponding schematic illustrations of BL (c) and PTL (d) after plating with 2 mAh cm<sup>-2</sup> of Li. e–j) In situ optical microscopy observation of Li plating behavior on BL (e–g) and PTL (h–j) after 0 min (e,h), 30 min (f,i), and 60 min (g,j) of deposition.

Besides the nucleation and growth overpotentials, the morphology of the plated lithium is also of vital importance. Here, SEM and in situ optical microscopy were combined to investigate the lithium plating behavior on the BL and PTL. As shown in Figure 2c, after depositing 2 mAh cm<sup>-2</sup> of lithium in carbonate ester based electrolyte, the surface of BL exhibits obvious dendrite growth with a chaotic structure. For PTL, it is clear that the PT layer well maintain its original morphology without lithium plating induced change (Figure S4, Supporting Information), indicating that the Li<sup>+</sup> passes through the PT layer and deposits on the PT layer/lithium interface. To obtain an intuitive observation for this, we then checked the morphology of the PTL after peeling off the PT layer. Different from the lithium dendrite growth on BL, the deposited lithium on PTL demonstrates a dendrite-free morphology with a much more uniform and smooth surface (Figure 2d), revealing that the PT layer can indeed effectively prevent lithium dendrite growth.

This can be further confirmed by using in situ optical microscopy to monitor the morphology evolution of the BL and PTL during lithium plating process (Figure 2e–j). Just after 30 min of deposition, the dendrite begins to appear at the cross-section of BL and then serious inhomogeneous lithium depositions aggregate on the BL surface as the deposition time prolongs (Figure 2e–g). In contrast, the PTL displays pretty smooth morphology with no observable dendrite growth and inconspicuous volume expansion during the whole plating process, indicating the lithium deposited under the PT layer and its guided uniform plating on the whole electrode (Figure 2h–j). As for the plating behavior in ether-based electrolyte, similar phenomenon of homogeneous lithium deposition and less volume expansion can be observed for the PTL (Figures S5–S7, Supporting Information), demonstrating the satisfying dendrite suppression effect of PT layer in both ether-based and carbonate ester based electrolytes.

Considering that the charge transfer and  $\text{Li}^+$  diffusion kinetics of the protection layer play a key role in obtaining a satisfying performance, time-dependence electrochemical impedance spectra (EIS) were employed to compare the impedance of BL and PTL based Li/Li symmetrical batteries with carbonate ester based electrolyte. In the EIS plot, the high frequency semicircle, mid-frequency semicircle, and low frequency region are associated with interfacial resistance ( $R_{\text{int}}$ ), charge transfer resistance ( $R_{\text{ct}}$ ), and  $\text{Li}^+$  diffusion process,<sup>[34]</sup> respectively. The values of the  $R_{\text{int}}$  and  $R_{\text{ct}}$  for BL or PTL based symmetrical batteries can be obtained by fitting the EIS curves to the equivalent circuit (Figure 3a–c). It is clear that the PTL based battery exhibits low  $R_{\text{int}}$  (4.203  $\Omega$ ) and  $R_{\text{ct}}$  (3.108  $\Omega$ ) values, while the  $R_{\text{int}}$  and  $R_{\text{ct}}$  for BL based battery are very large, about 6.8 and 7.7 times of those of PTL based battery (Figure 3c), indicating that the PT layer can enable high ion transport and fast charge transfer kinetics. Even after resting for 7 days, different from the significant increase of the  $R_{\text{int}}$  (57.15  $\Omega$ ) and  $R_{\text{ct}}$  (46  $\Omega$ ) for BL based battery, the  $R_{\text{int}}$  (5.659  $\Omega$ ) and  $R_{\text{ct}}$  (9.024  $\Omega$ ) for PTL based battery only experience a small increase and still maintain a low value, revealing that the PT layer can facilitate a stable electrode/electrolyte

interface with much reduced parasitic reactions.<sup>[35,36]</sup> The other thing to note is that the low frequency range slope of the PTL based battery is also much higher than that of BL based battery, demonstrating an improved  $\text{Li}^+$  diffusion characteristics.<sup>[16]</sup> Moreover, in ether-based electrolyte, the PTL-based battery still exhibits much lower impedance with high ion transport and fast charge transfer kinetics both before and after storing for 9 days (Figure S8, Supporting Information).

The long-term stability of the BL and PTL were then evaluated by conducting galvanostatic plating/stripping cycling tests on BL and PTL based Li/Li symmetrical batteries. In carbonate ester based electrolyte, the symmetrical batteries with PTL exhibit lower overpotentials and longer cycling stabilities of about 1400 and 800 h than those of the batteries with BL under the current densities of 0.5 and 1  $\text{mA cm}^{-2}$  (Figures S9 and S10, Supporting Information). Even at a high current density of 3  $\text{mA cm}^{-2}$ , the battery with PTL can still run for about 350 cycles with less polarization compared with the battery with BL (Figure S11, Supporting Information). The excellent cycling stability of the PTL based batteries can be attributed to the PT layer enabled dendrite-free lithium plating/stripping

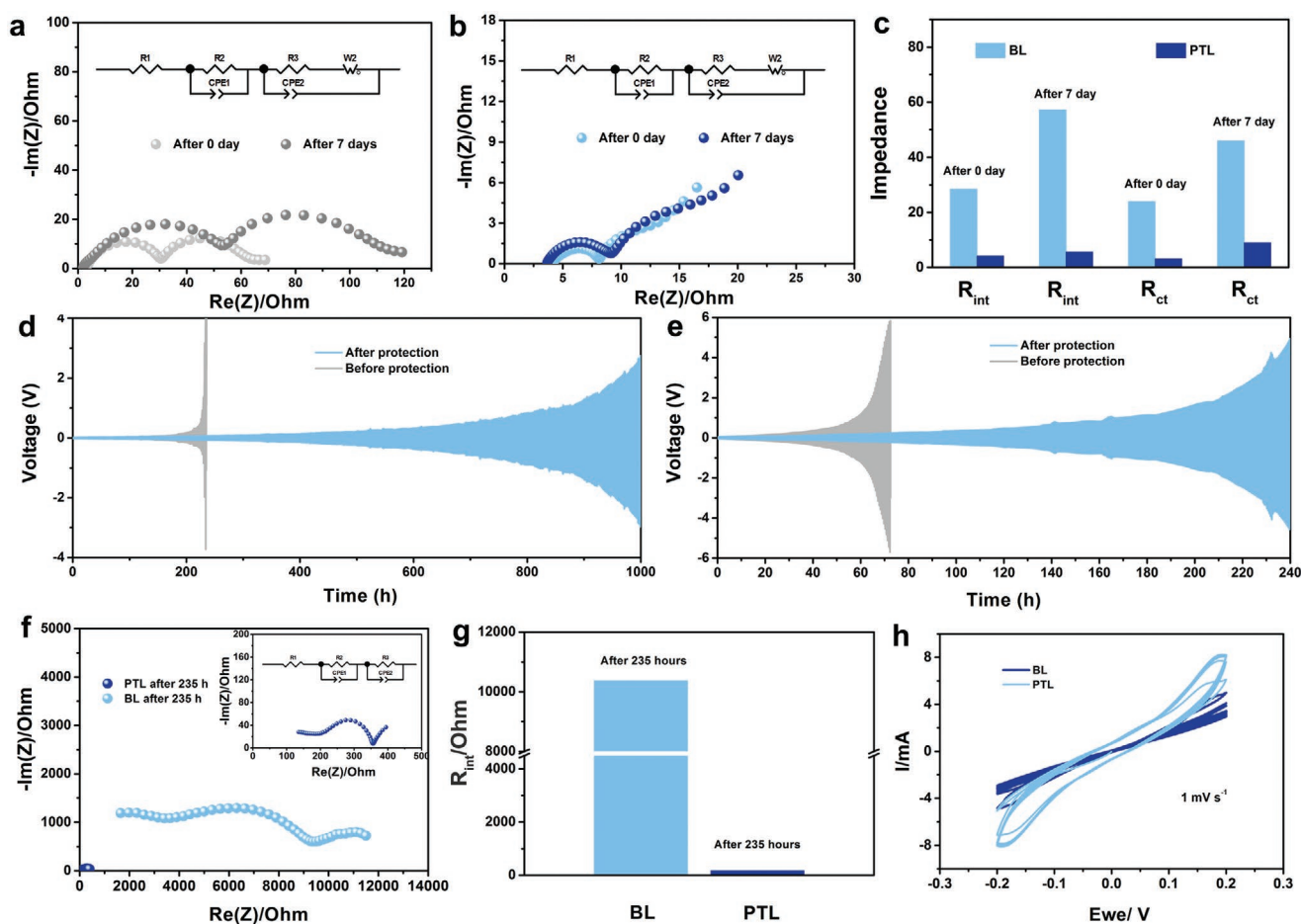


**Figure 3.** a,b) Electrochemical impedance spectra (EIS) curves of Li/Li symmetrical batteries with BL (a) and PTL (b) as electrodes before and after staying for 7 days and c) corresponding comparison of  $R_{\text{int}}$  and  $R_{\text{ct}}$  impedance values. d,e) Long-term cycling performance of BL and PTL based Li/Li symmetrical batteries with 1 M  $\text{LiCF}_3\text{SO}_3$  in TEGDME electrolyte at current densities of 0.1  $\text{mA cm}^{-2}$  (d) and 0.4  $\text{mA cm}^{-2}$  (e). f) EIS curves of Li/Li symmetrical batteries with BL and PTL after cycling for 235 h at a current density of 0.1  $\text{mA cm}^{-2}$ , and g) corresponding  $R_{\text{int}}$  value comparison. h) Cyclic voltammetry (CV) curves of Li/Li symmetrical batteries with BL and PTL electrodes scanned at a fixed rate of 1  $\text{mV s}^{-1}$ .

and stable electrode/electrolyte interface, which make the PTL based battery exhibit a much lower impedance than the BL based battery after cycling for 70 cycles under  $3 \text{ mA cm}^{-2}$  (Figure S12, Supporting Information). Importantly, the protection effects of the PT layer on lithium anode are more obvious in ether-based electrolyte, which prolong the cycling stability from 235 to 1000 h at a lower current density of  $0.1 \text{ mA cm}^{-2}$  (Figure 3d). Increased the current density to  $0.4 \text{ mA cm}^{-2}$ , the battery with PTL still shows nearly three times longer cycle life than that of BL based battery (Figure 3e). The short lifetime of the BL based battery is due to the continuous dendrite growth induced repeated damage and reestablishment of the SEI film, which produces a thick SEI film, and thus a high  $R_{\text{int}}$  up to  $10\,375 \, \Omega$  after cycling for 235 h (Figure 3f,g). Such a high  $R_{\text{int}}$  makes the ion transport become very difficult and causes the sudden death of the battery. Whereas, the PT layer endowed stable electrode/electrolyte interface makes the PTL based battery exhibit a 61-fold lower  $R_{\text{int}}$  than that of the BL based battery, as a result, significantly boosting the cycling stability of the PTL based battery.

In order to further verify the advantage of the PTL, exchange current density ( $j^0$ ), another important electrochemical kinetics

parameter, was checked. Since  $j^0$  is proportional to the gradient of the cyclic voltammetry (CV) curves, the larger gradient of the CV curves of the PTL based battery indicates it has a higher  $j^0$  in both ether-based and carbonate ester based electrolytes (Figure 3h and S13, Supporting Information), meaning that the lithium plating/stripping process can be proceeded at a higher speed and a lower polarization, which is consistent with the above mentioned small impedance and lithium plating/stripping overpotential of the PTL based battery.<sup>[34–36]</sup> The higher  $j^0$  confirms that the introduction of PT layer can accelerate the charge transfer and ion diffusion processes thus an enhanced Li plating/stripping kinetic.

To reveal the mechanism of the PT layer on regularizing the lithium deposition process, first-principles density functional theory based (DFT) calculations were conducted to analyze the interactions between  $\text{Li}^+$  and LiF, LiF/C, or PT layer. The  $\text{Li}^+$  adsorption energy and charge density distribution of PT layer, LiF/C, and LiF are summarized in Figure 4a,b and Figures S14 and S15 (Supporting Information). Compared with LiF and carbon layer, the C–F bonds in the F-doped carbon make it has the highest adsorption energy to  $\text{Li}^+$  ( $-3.87 \text{ eV}$ ) and form negative charge centers, which can preuniform Lewis acid  $\text{Li}^+$  and effectively assist to form homogeneous  $\text{Li}^+$  flux for further

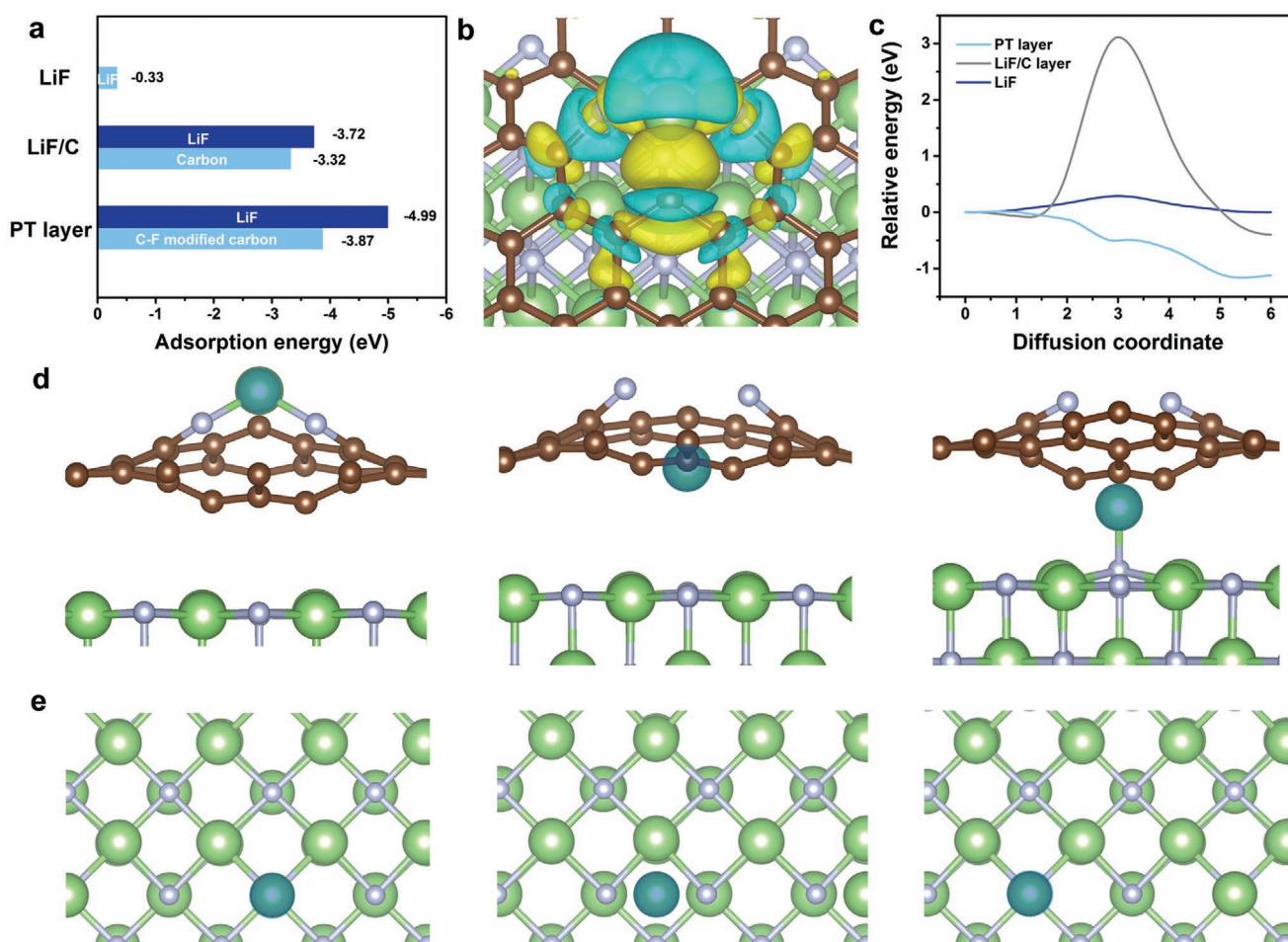


**Figure 4.** a) Adsorption energies of  $\text{Li}^+$  on different species. b) Charge density difference plot of a  $\text{Li}^+$  on the F-doped carbon layer in the PT layer. c)  $\text{Li}^+$  diffusion energy barriers of different species. d,e)  $\text{Li}^+$  diffusion path through F-doped carbon layer (d) and the LiF (100) facet in the PT layer (e). Li, F, and C elements are represented by green, light purple, and brown spheres, respectively. The migrating  $\text{Li}^+$  is represented by a cyan sphere.

deposition. Surprisingly, with the presence of F-doped carbon, the Li<sup>+</sup> adsorption energy of LiF is 15-fold higher than that of pure LiF (−4.99 vs −0.33 eV), indicating that the F-doped carbon can change the electron configuration of LiF, so increase the affinity between Li<sup>+</sup> and LiF. Besides the Li<sup>+</sup> adsorption energy, the diffusion energy barrier of Li<sup>+</sup> should be also considered. If it is too high, it may introduce lithium accumulation. As shown in Figure 4c, the PT layer exhibits a greatly reduced Li<sup>+</sup> diffusion energy barrier, which is 3 eV lower than that of pure carbon, suggesting that Li<sup>+</sup> can almost self-diffusion in the PT layer by just overcoming a small energy barrier. The entire functional mechanism of the PT layer is schemed in Figure 4d,e. The Li<sup>+</sup> in the electrolyte is first homogeneously captured by the C–F bonds in the upper F-doped carbon layer, then nearly spontaneously diffuses to the surface of LiF, and finally overcomes 0.29 eV diffusion energy barrier to plate on lithium metal anode. This is in well agreement with the above experimental results, the stronger adsorption and lower diffusion barrier of Li<sup>+</sup> on PT layer effectively promote uniform Li<sup>+</sup> flux and smooth lithium deposition. The calculation results also

demonstrate that the PT layer integrates the homogenizing Li<sup>+</sup> flux function of F-doped carbon and the fast Li<sup>+</sup> diffusion ability of LiF together as well as endows F-doped carbon and LiF with Li<sup>+</sup> quasi-self-diffusion and strong Li adsorption capability.

In light of the ultrahigh energy density of Li–O<sub>2</sub> battery and its lack of stable lithium metal anode, we employed PTL to assemble Li–O<sub>2</sub> batteries to demonstrate its practical application ability. Figure S18 (Supporting Information) shows the CV curve of Li–O<sub>2</sub> battery with PTL. The cathodic and anodic peaks represent the typical O<sub>2</sub> reduction and evolution reactions in Li–O<sub>2</sub> batteries, consisting with the reported literature.<sup>[38,39]</sup> Galvanostatic charge–discharge cycling testing of Li–O<sub>2</sub> batteries with BL and PTL was then evaluated. As shown in Figure 5a,b, the Li–O<sub>2</sub> battery with PTL can achieve a long cycling stability of 180 cycles, much than two times of the battery with BL, which can only run 78 cycles under the same condition. This difference can be ascribed to the improved stability of the PT layer protected lithium metal anode.<sup>[18,19]</sup> To confirm this, the morphology evolution of BL and PTL after multiple cycles has been compared. From Figure S19 (Supporting Information) we can

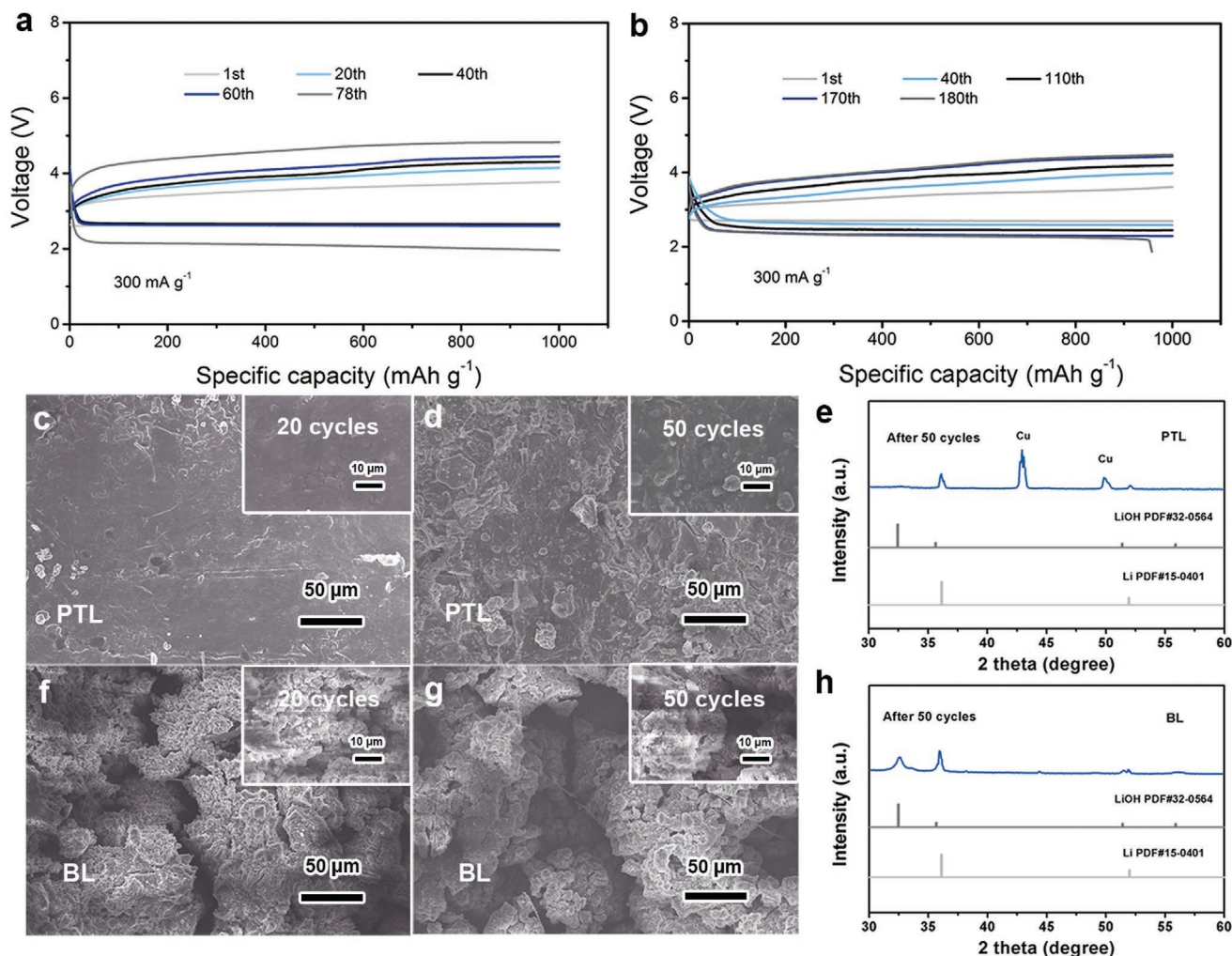


**Figure 5.** a,b) Long-term cycling performance of Li–O<sub>2</sub> batteries with BL (a) and PTL (b) as anodes. c,d) SEM images of PTL after cycling in Li–O<sub>2</sub> batteries for 20 cycles (c) and 50 cycles (d). e) X-ray diffraction (XRD) patterns of PTL after cycling in Li–O<sub>2</sub> batteries for 50 cycles. f,g) SEM images of BL after cycling in Li–O<sub>2</sub> batteries for 20 cycles (f) and 50 cycles (g). h) XRD patterns of BL after cycling in Li–O<sub>2</sub> batteries for 50 cycles.

see that, the PTL maintains the surface morphology just like the pristine condition after 50 cycles, revealing the good stability of the PT layer. For getting the morphology information of the lithium under PT layer, we peeled off the PT layer and exposed the lithium surface. As expected, the lithium under PT layer has a relative smooth surface without obvious dendrite growth and corrosion reaction induced morphology change (Figure 5c,d), indicating that the PT layer can inhibit lithium dendrite growth and isolating lithium from attacking by the rigorous environment in Li–O<sub>2</sub> batteries. Whereas, the BL exhibits serious corrosion morphology with a lot of sags and crests (Figure 5f,g), which can be regarded as the culprit of battery failure. To further reveal the protection effect of PT layer, XRD was used to characterize the composition of the cycled lithium anodes.<sup>[37]</sup> Figure 5e,h shows that there is almost no observable LiOH peaks on the PTL after 50 cycles (Figure S20, Supporting Information), while the LiOH peaks on the cycled BL are quite strong, implying that the PT layer can endow a satisfying anticorrosion effect on the lithium anode. We even use the cycled BL and PTL to assemble symmetrical batteries and find that the PTL based battery displays a much lower impedance than that of the BL based battery (Figure S22, Supporting Information), again verifying the much improved stability of the lithium anode with the assistance of PT layer. Moreover, the discharged cathode in the PTL based Li–O<sub>2</sub> battery is also evaluated and it shows typical toroid-like crystalline Li<sub>2</sub>O<sub>2</sub> (Figure S23, Supporting Information), which is consistent with previous literatures.<sup>[38,39]</sup> Besides, at the current density of 200 mA g<sup>-1</sup>, the Li–O<sub>2</sub> batteries with PTL behave a satisfying discharge capacity of 5957.9 mAh g<sup>-1</sup> (Figure S24, Supporting Information) and the rate performance is also stable and satisfying (Figure S25, Supporting Information). All these results demonstrate that the PTL can effectively improve the cycling stability of Li–O<sub>2</sub> batteries without affecting the reaction mechanism.

In summary, a one-step in situ reaction between lithium sheet and PTFE micropowders has been designed to generate a multifunctional complementary LiF/F-doped carbon gradient protection layer that seamlessly coated on lithium metal anode, thus resolving the long-lasting dendrite growth and corrosion challenges of lithium anodes in Li–O<sub>2</sub> batteries and enhancing the electrochemical performance. Revealed by first-principle calculations, this gradient protection layer integrates the homogenizing Li<sup>+</sup> flux function of F-doped carbon and the fast Li<sup>+</sup> diffusion ability of LiF together, meanwhile, the two phases can complementary each other by decreasing the Li<sup>+</sup> diffusion barrier of F-doped carbon and increasing the Li<sup>+</sup> adsorption energy of LiF. As a result, this protection layer enables faster charge/mass transfer kinetics and dendrite free lithium plating/stripping at lower nucleation/growth energy barriers in symmetrical batteries with both ether-based and carbonate ester based electrolytes. Furthermore, a successful practical application of the PTL has been realized in Li–O<sub>2</sub> batteries, in which the fatal dendrite growth and parasitic reactions on lithium metal anode are greatly remitted and the cycling stability is significantly improved (180 cycles). This unique anode protection design strategy opens a new avenue for practical study of alkali metal anodes in metal based batteries.

## Supporting Information

Supporting Information is available from the Wiley Online Library or from the author.

## Acknowledgements

Y.Y., G.H., and J.-Z.W. contributed equally to this work. This work was financially supported by the National Key R&D Program of China (2016YFB0100103), the National Natural Science Foundation of China (21725103), the Strategic Priority Research Program of the Chinese Academy of Sciences (XDA21010210), the Jilin Province Science and Technology Development Plan Funding Project (20180101203)C, 20200201079)C, and the Changchun Science and Technology Development Plan Funding Project (19SS010). We also appreciated the kind help from National & local united engineering lab for power battery in Northeast Normal University.

## Conflict of Interest

The authors declare no conflict of interest.

## Keywords

anticorrosion, dendrite suppression, Li–O<sub>2</sub> battery, lithium metal anode, protection layer

Received: June 18, 2020

Revised: June 26, 2020

Published online: August 9, 2020

- [1] C. Xia, C. Y. Kwok, L. F. Nazar, *Science* **2018**, 361, 777.
- [2] G. H. Lee, M. C. Sung, J. C. Kim, H. J. Song, D. W. Kim, *Adv. Energy Mater.* **2018**, 8, 1801930.
- [3] X. Lin, R. Yuan, Y. Cao, X. Ding, S. Cai, B. Han, Y. Hong, Z. Zhou, X. Yang, L. Gong, M. Zheng, Q. Dong, *Chem* **2018**, 4, 2685.
- [4] T. Or, S. W. D. Gourley, K. Kaliyappan, A. P. Yu, Z. W. Chen, *Carbon Energy* **2020**, 2, 6.
- [5] J. X. Wu, Y. L. Cao, H. M. Zhao, J. F. Mao, Z. P. Guo, *Carbon Energy* **2019**, 1, 57.
- [6] H. Xu, C. Peng, Y. Yan, F. Dong, H. Sun, J. Yang, S. Zheng, *Carbon Energy* **2019**, 1, 276.
- [7] D. Aurbach, B. D. McCloskey, L. F. Nazar, P. G. Bruce, *Nat. Energy* **2016**, 1, 16128.
- [8] X. Lei, X. Liu, W. Ma, Z. Cao, Y. Wang, Y. Ding, *Angew. Chem., Int. Ed.* **2018**, 57, 16131.
- [9] X. Wang, Y. Li, X. Bi, L. Ma, T. Wu, M. Sina, S. Wang, M. Zhang, J. Alvarado, B. Lu, A. Banerjee, K. Amine, J. Lu, Y. S. Meng, *Joule* **2018**, 2, 2381.
- [10] B. Liu, W. Xu, J. Tao, P. Yan, J. Zheng, M. H. Engelhard, D. Lu, C. Wang, J. G. Zhang, *Adv. Energy Mater.* **2018**, 8, 1702340.
- [11] S. Choudhury, C. T. C. Wan, W. I. A. Sadat, Z. Y. Tu, S. Lau, M. J. Zachman, L. F. Kourkoutis, L. A. Archer, *Sci. Adv.* **2017**, 3, e1602809.
- [12] X. Lin, Q. Sun, K. D. Davis, R. Li, X. Sun, *Carbon Energy* **2019**, 1, 141.
- [13] T. Kang, Y. Wang, F. Guo, C. Liu, J. Zhao, J. Yang, H. Lin, Y. Qiu, Y. Shen, W. Lu, L. Chen, *ACS Cent. Sci.* **2019**, 5, 468.
- [14] Y. Guo, P. Niu, Y. Liu, Y. Ouyang, D. Li, T. Zhai, H. Li, Y. Cui, *Adv. Mater.* **2019**, 31, 1900342.

- [15] Y. Sun, Y. Zhao, J. Wang, J. Liang, C. Wang, Q. Sun, X. Lin, K. R. Adair, J. Luo, D. Wang, R. Li, M. Cai, T. K. Sham, X. Sun, *Adv. Mater.* **2019**, *31*, 1806541.
- [16] E. Cha, M. D. Patel, J. Park, J. Hwang, V. Prasad, K. Cho, W. Choi, *Nat. Nanotechnol.* **2018**, *13*, 337.
- [17] X. Shen, Y. Li, T. Qian, J. Liu, J. Zhou, C. Yan, J. B. Goodenough, *Nat. Commun.* **2019**, *10*, 900.
- [18] Q. C. Liu, J. J. Xu, S. Yuan, Z. W. Chang, D. Xu, Y. B. Yin, L. Li, H. X. Zhong, Y. S. Jiang, J. M. Yan, X. B. Zhang, *Adv. Mater.* **2015**, *27*, 5241.
- [19] J. J. Xu, Q. C. Liu, Y. Yu, J. Wang, J. M. Yan, X. B. Zhang, *Adv. Mater.* **2017**, *29*, 1606552.
- [20] X. Y. Zhang, R. J. Lv, A. X. Wang, W. Q. Guo, X. J. Liu, J. Y. Luo, *Angew. Chem., Int. Ed.* **2018**, *57*, 15028.
- [21] G. Huang, J. Han, F. Zhang, Z. Wang, H. Kashani, K. Watanabe, M. Chen, *Adv. Mater.* **2019**, *31*, 1805334.
- [22] L. Suo, W. Xue, M. Gobet, S. G. Greenbaum, C. Wang, Y. Chen, W. Yang, Y. Li, J. Li, *Proc. Natl. Acad. Sci. USA* **2018**, *115*, 1156.
- [23] X. L. Fan, X. Ji, F. D. Han, J. Yue, J. Chen, L. Chen, T. Deng, J. J. Jiang, C. S. Wang, *Sci. Adv.* **2018**, *4*, eaau9245.
- [24] J. Xie, L. Liao, Y. J. Gong, Y. B. Li, F. F. Shi, A. Pei, J. Sun, R. F. Zhang, B. Kong, R. Subbaraman, J. Christensen, Y. Cui, *Sci. Adv.* **2017**, *3*, eaao3170.
- [25] J. Zhao, L. Liao, F. Shi, T. Lei, G. Chen, A. Pei, J. Sun, K. Yan, G. Zhou, J. Xie, C. Liu, Y. Li, Z. Liang, Z. Bao, Y. Cui, *J. Am. Chem. Soc.* **2017**, *139*, 11550.
- [26] X. B. Cheng, T. Z. Hou, R. Zhang, H. J. Peng, C. Z. Zhao, J. Q. Huang, Q. Zhang, *Adv. Mater.* **2016**, *28*, 2888.
- [27] Z. Liang, G. Zheng, C. Liu, N. Liu, W. Li, K. Yan, H. Yao, P. C. Hsu, S. Chu, Y. Cui, *Nano Lett.* **2015**, *15*, 2910.
- [28] C. Liu, P. C. Hsu, H. W. Lee, M. Ye, G. Zheng, N. Liu, W. Li, Y. Cui, *Nat. Commun.* **2015**, *6*, 6205.
- [29] C. Huang, J. Xiao, Y. Shao, J. Zheng, W. D. Bennett, D. Lu, L. V. Saraf, M. Engelhard, L. Ji, J. Zhang, X. Li, G. L. Graff, J. Liu, *Nat. Commun.* **2014**, *5*, 3015.
- [30] C. Zhang, Z. J. Huang, W. Lv, Q. B. Yun, F. Y. Kang, Q. H. Yang, *Carbon* **2017**, *123*, 744.
- [31] F. Ren, Z. Peng, M. Wang, Y. Xie, Z. Li, H. Wan, H. Lin, D. Wang, *Energy Storage Mater.* **2019**, *16*, 364.
- [32] W. Zhang, S. Zhang, L. Fan, L. Gao, X. Kong, S. Li, J. Li, X. Hong, Y. Lu, *ACS Energy Lett.* **2019**, *4*, 644.
- [33] A. Pei, G. Zheng, F. Shi, Y. Li, Y. Cui, *Nano Lett.* **2017**, *17*, 1132.
- [34] Q. Xu, Y. Yang, H. Shao, *Electrochim. Acta* **2018**, *259*, 534.
- [35] Z. Tu, S. Choudhury, M. J. Zachman, S. Wei, K. Zhang, L. F. Kourkoutis, L. A. Archer, *Nat. Energy* **2018**, *3*, 310.
- [36] Q. Zhao, Z. Tu, S. Wei, K. Zhang, S. Choudhury, X. Liu, L. A. Archer, *Angew. Chem., Int. Ed.* **2018**, *57*, 992.
- [37] J. L. Shui, J. S. Okasinski, P. Kenesei, H. A. Dobbs, D. Zhao, J. D. Almer, D. J. Liu, *Nat. Commun.* **2013**, *4*, 2255.
- [38] B. M. Gallant, D. G. Kwabi, R. R. Mitchell, J. Zhou, C. V. Thompson, Y. Shao-Horn, *Energy Environ. Sci.* **2013**, *6*, 2518.
- [39] R. R. Mitchell, B. M. Gallant, Y. Shao-Horn, C. V. Thompson, *J. Phys. Chem. Lett.* **2013**, *4*, 1060.
- [40] C. Quarti, A. Milani, C. Castiglioni, *J. Phys. Chem. B* **2013**, *117*, 706.